Influence of CH_4 partial pressure on the microstructure of sputter-deposited tungsten carbide thin films

2006 J. Phys.: Condens. Matter 18 1913

(http://iopscience.iop.org/0953-8984/18/6/008)

INSTITUTE OF PHYSICS PUBLISHING JOURNAL OF PHYSICS: CONDENSED MATTER

J. Phys.: Condens. Matter **18** (2006) 1913–1925 doi:10.1088/0953-8984/18/6/008

Influence of CH_4 partial pressure on the microstructure of sputter-deposited tungsten carbide thin films

K Abdelouahdi[1], C Sant[1], F Miserque[2], P Aubert[1], Y Zheng[3], C Legrand-Buscema[1] and J Perrière[3]

[1] Laboratoire d'Etude des Milieux Nanométriques, Bâtiment Maupertuis 1, rue du Père Jarlan, 91025 Evry cedex, France
[2] CEA–Saclay/DEN/DPC/SCP/Laboratoire de Réactivité des Surfaces et Interfaces, Bâtiment 391, 91191 Gif sur Yvette, France
[3] Institut des NanoSciences de Paris, Université Paris VI, Campus Boucicaut, 140 rue de Lourmel, 75015 Paris, France

E-mail: karima.abdelouahdi@uni-evry.fr and catherine.sant@chimie.univ-evry.fr

Received 25 July 2005
Published 24 January 2006
Online at stacks.iop.org/JPhysCM/18/1913

Abstract

Tungsten carbide thin films have been prepared by reactive rf sputtering from a tungsten target in various Ar–CH_4 mixtures. The composition, structure, microstructure and chemical state of the films have been investigated by the complementary use of RBS, NRA, XRD, GIXRD, TEM and XPS analyses. These characteristics of the films were then correlated to their mechanical properties determined by hardness (H), Young's modulus (E_r) and friction coefficient measurements. Under low CH_4 pressures, the formation of a mixture of nanocrystalline WC_{1-x} and W_2C phases has been observed. A pure WC_{1-x} phase was observed in films having a composition close to $W_1C_{0.9}$. With increasing CH_4 pressure, the amount of carbon in the films increases, leading to a progressive amorphization of tungsten carbide deposited layers. Nanocomposite films appeared to be formed, with WC_{1-x} nanograins (<3 nm) dispersed in an amorphous carbon matrix. The film deposited at 30% of CH_4 exhibits a-C:H phase. The nature of the phases present in the films plays an important role on their mechanical properties, as shown by the wide domain of variation of the films' hardness (between 22 and 5.5 GPa) and the plastic deformation parameter H^3/E_r^2 (between 0.08 and 0.04).

1. Introduction

Transition metal carbides like tungsten carbide have a high technological interest due to many of their specific physical and mechanical properties [1]. For example, tungsten carbide exhibits high melting point, extreme hardness, low coefficient of friction, chemical inertness, oxidation resistance and good electrical conductivity. These properties make this material an

ideal candidate for many industrial application like wear-resistant coatings, and cutting and drilling tools. In addition, the rare combination of strong bonding and metallic conductivity makes tungsten carbide an attractive material for high temperature contacts or as a conductive protective layer in sensor applications.

According to the phase diagram of the stable binary W–C system investigated by many authors [2–4], three different carbides exist: tungsten monocarbide W_1C_1(WC), with a simple hexagonal structure, which is the only thermodynamically stable phase at room temperature in a narrow domain [5]; a cubic carbide that is referred to as WC_{1-x}; and a second hexagonal carbide W_2C. More recently, Demetriou *et al* (2002) [6] have reported a computed metastable phase equilibrium of the W–C system. They found that under some specific processes, W_2C and/or WC_{1-x} can crystallize at room temperature instead of the WC phase.

In agreement with these results, tungsten carbide thin films often have the WC_{1-x} [7–13, 16–28] and W_2C [7, 10, 11, 13] crystalline structures. The WC phase is the less observed one [7, 8, 10] in thin films. Moreover, the x value (in the WC_{1-x} phase) which is measured in tungsten carbide thin films can reach 0, i.e. a value lower than the one reported in the phase diagram. This decrease of the x value indicates that the incorporation of carbon in the WC_{1-x} lattice is higher than that predicted by the phase diagram and induces an increase of the lattice parameter [7].

Due to the importance of the carbon concentration on the nature of the tungsten carbide phases, we have studied in this work the formation of tungsten carbide thin films by rf sputtering from a W target under various methane/argon gas mixtures. The composition and structure of the films have thus been investigated as a function of CH_4 pressure. Then, the mechanical properties of the tungsten carbide deposited layers have been correlated to the nature of the tungsten carbide crystalline phases present in these films.

2. Experimental details

2.1. Deposition process

Tungsten carbide layers with a wide range of W/C concentration ratio were deposited on (100) oriented silicon wafers by reactive rf sputtering from a pure tungsten target (5 N) in an Ar/CH_4 gas mixture. The native SiO_2 layer always present at the surface of the Si wafer was not removed and thus it prevents any epitaxial growth of the tungsten carbide thin films on the Si single crystal substrates. The samples were placed 7 cm away from the target, and heated to 150 °C. The overall sputtering pressure was fixed at 0.25 Pa for all the experiments, and the sputtering rf power was 200 W, leading to a −400 V self-bias. Various methane partial pressures were investigated: 1, 2, 3, 4, 5 and 30% of total pressure. The corresponding samples have been called $\boldsymbol{a}$, $\boldsymbol{b}$, $\boldsymbol{c}$, $\boldsymbol{d}$, $\boldsymbol{e}$ and $\boldsymbol{f}$, respectively. For transmission electron microscopy analysis, additional samples were deposited at 2% of CH_4 (called $\boldsymbol{b}'$) and 5% of CH_4 (called $\boldsymbol{e}'$) on carbon grids with a thickness of about 25 nm. The film thickness was approximately 360 nm for mechanical studies and less than 100 nm for XRR (x-ray reflectivity) studies.

2.2. Microstructural and mechanical characterizations

The film composition was determined by combining Rutherford backscattering spectroscopy (RBS) and nuclear reactions analysis (NRA). The measurements of carbon and oxygen contents by NRA were performed respectively through the $^{12}C(d, p)^{13}C$ and $^{16}O(d, p)^{17}O$ nuclear reactions induced in the samples by deuteron beams of 960 keV for carbon and 860 keV for oxygen. The film thickness and the tungsten and carbon concentrations were deduced from the RBS spectra by using the RUMP simulation program.

The structure of the samples was investigated by x-ray diffraction, using a Bruker D8 advance x-ray diffractometer (Cu Kα radiation) equipped with a Goble mirror. The investigations were carried out by both Bragg–Brentano geometry (XRD) and grazing incidence mode (GIXRD). In both cases the scanning angle of the detector, 2θ, was varied within the range 30°–80° by a step of 0.04°. For XRD diagrams the (004) peak of the Si single crystal substrate masks diffraction peaks from the film which could be present in the 60° to 75° range; then XRD patterns are given between 30° and 60°. For GIXRD, the grazing angle was 1.5°, which leads to analysis of the total layer thickness. In this case, the angle between the incident x-ray beam and Si(004) plane orientation does not satisfy Bragg's law. The Si(004) peak is no longer present, which allows one to observe whether peaks are present in the 60° to 80° 2θ range. Then GIXRD patterns are given between 30° and 80°. The density, thickness and roughness of films thinner than 100 nm were determined by simulation of x-ray reflectivity (XRR) patterns using Refsim software.

The chemical states of carbon and tungsten in the thin film were examined using x-ray photoelectron spectroscopy (XPS). XPS spectra were recorded with a VG ESCALAB 220i XL spectrometer (Thermo Electron Society). The x-ray source used is the monochromatic Kα ray of aluminium (1486.6 eV). The beam diameter is around 1×1 mm^2. The pass energy was 20 eV. The spectrometer is calibrated in energy to the silver Fermi level (0 eV) and to the $3d_{5/2}$ electronic level of silver (368.3 eV). The residual pressure in the XPS chamber is around 10^{-10} mbar. Prior to analysis, the samples were sputtered by Ar^+ ions in order to remove the oxide layer formed at the surface. The sputtering time was adjusted in order to suppress the O 1s peak characteristics of oxidized surface layers. The data processing and deconvolution of photoelectron peaks were done by AVANTAGE packages supplied with the instrument.

TEM images and electron diffractions patterns were obtained using a JEM 2100F microscope operating at 200 kV.

The mechanical properties of the tungsten carbide films were determined through hardness, reduced Young's modulus and friction coefficient measurements which were carried out using a Hysitron triboscope nanomechanical system with a maximal force equal to 10 mN. This device is connected to a digital instruments D 3100 AFM. A pyramidal diamond Berkovich tip was used for visualization and tests. Hardness H and reduced Young's modulus E_r values were deduced by the Oliver and Pharr analysis method (1992) [27]. In order to avoid the influence of the substrate, the penetration depth was always kept below 10% of the layer thickness. All the data given in this study correspond to an average of 20 measurements. The scratch tests were performed by varying the normal load from 0 to 1000 μN with a speed equal to 33 μN s^{-1}. The scratch length was 10 μm.

3. Results and discussions

3.1. Composition and structure

Figure 1 represents the evolution of the C/W concentration ratio as a function of CH_4 pressure during the sputtering process, and table 1 summarizes the composition as a function of deposition conditions. As expected, the carbon concentration in the films increases with increasing methane pressure: the C/W concentration ratio in the films increases from 0.76 to 12 with the methane concentration varying in the range 1–30% of total gas pressure (see figure 1). In fact the increase in the methane pressure leads both to the increase of the carbon species which can be incorporated in the growing film, and to the decrease of the argon ionic species for the sputtering of the tungsten target. These two phenomena are at the origin of the observed increase in carbon content of the films, and this increase is also accompanied by a

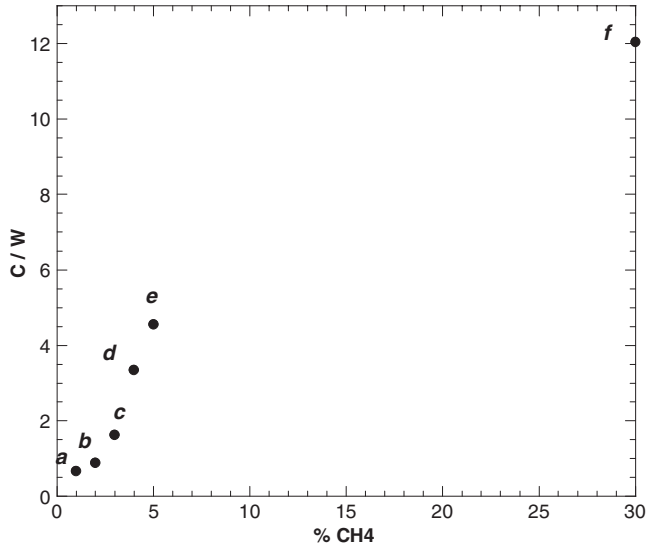

Figure 1. Tungsten and carbon concentrations in W–C films versus CH_4 concentration (%).

Table 1. Composition of the W–C films deposited under 1, 2, 3, 4, 5 and 30% CH_4.

Sample	CH_4 (%)	Composition
a	1	$WC_{0.75}$
b	2	$WC_{0.9}$
c	3	$WC_{1.65}$
d	4	$WC_{3.6}$
e	5	$WC_{4.8}$
f	30	$W_1C_{12}H_{12}$

reduction of the film density from 15.8 (close to the WC one (15.7) and WC_{1-x} one (17.2)) for the sample ***a*** to 3.7 for the sample ***f*** close to the carbon graphite one (3.5).

It has to be noticed that the carbon concentrations deduced from the RUMP simulation of the RBS spectra were in perfect agreement with the carbon content measured by NRA for all the samples, except the one obtained at the highest methane pressure (film ***f***). The reason why is that at this high methane pressure the phenomenon of plasma assisted deposition of amorphous hydrogenated carbon (a-C:H) is present during the sputtering process. In these conditions a high hydrogen incorporation in the film is expected, and to obtain the best fit of the RBS spectrum corresponding to this sample, a high hydrogen concentration (48%) was added to the tungsten carbide. For all the other samples the maximum hydrogen concentration in the film to fit the experimental RBS spectra was always lower than 2%.

From figure 1 and table 1, it can be deduced that in films ***a*** and ***b*** the carbon content is not sufficient to reach the ideal WC stoichiometric composition, and these films may be composed of a mixture of the WC_{1-x} and W_2C phases. In the case of the films ***c***, ***d***, ***e*** and ***f*** the carbon concentration is high enough to allow the presence of three possible phases: WC, WC_{1-x} and a carbon-rich one.

Typical XRD patterns recorded on tungsten carbide thin films are displayed in figure 2. Broad (FWHM $>$ 4°) and asymmetric peaks are observed, indicating the presence of crystallites with a reduced size and lattice defects in the films. A pseudo-Voigt function has

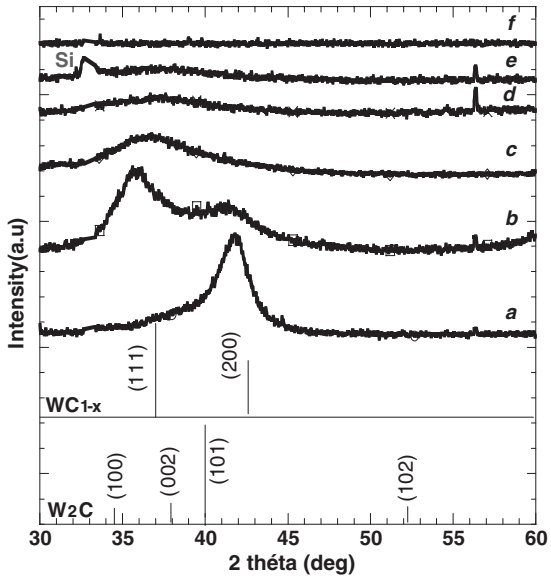

Figure 2. XRD patterns of coatings ***a***, ***b***, ***c***, ***d***, ***e*** and ***f*** respectively deposited under 1, 2, 3, 4, 5 and 30% CH_4 and calculated relative peak intensities of WC_{1-x} and W_2C phases.

Table 2. Calculated theoretical peak intensities of WC_{1-x} and W_2C phases for $x = 0.1$.

WC_{1-x} ($x = 0.1$)		W_2C	
(*hkl*)	*I*	(*hkl*)	*I*
(111)	100	(100)	22
(200)	59	(002)	24
(220)	36	(101)	100
(311)	34	(102)	16
(222)	11	(110)	17
		(103)	16
		(200)	2
		(112)	17
		(201)	13

been used to fit the diffraction peaks of the samples ***a*** and ***b***, while the peaks in the other patterns are too large to precisely determine the peak's position and perform good fits. The films ***a*** and ***b*** exhibit two diffraction peaks at $2\theta = 35.8°$ and 41.5°. These peaks can be attributed to the (111) and (200) peaks of the WC_{1-x} phase. An increase of the WC_{1-x} phase lattice parameter, related to an increase of the carbon content, leads to a shift of the peak positions towards lower angles (see figure 2).

Interesting information can be drawn from the ratio of peak intensities. In fact the theoretical peak intensities have been calculated for the WC_{1-x} and W_2C phases, and the results are reported in table 2 and figures 2 and 3. The films are polycrystalline with a rather small size of the crystallites, and thus a preferential orientation does not seem *a priori* likely. However, in the case of the film ***a***, the $I_{(200)}/I_{(111)}$ intensity ratio (i.e. 11) is twenty times higher than the calculated one (0.59 for $x = 0.1$). This shows that the population of (200) oriented crystallites is higher than that it would be for a pure polycrystalline film with random orientations. XRD

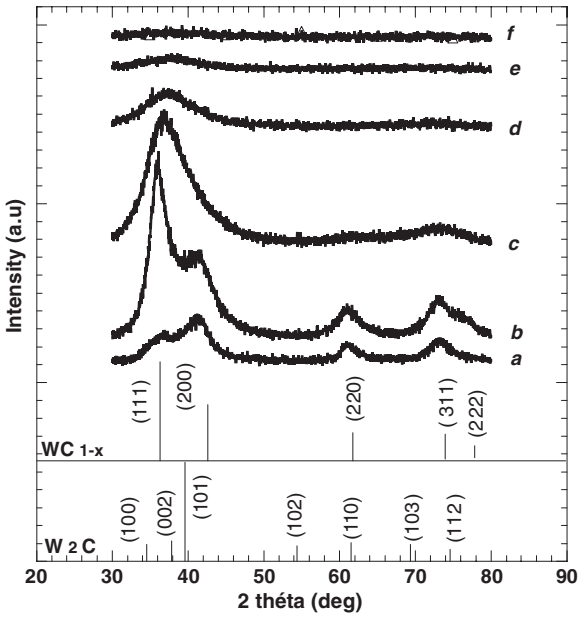

Figure 3. GIXRD patterns of coatings ***a***, ***b***, ***c***, ***d***, ***e*** and ***f*** respectively deposited under 1, 2, 3, 4, 5 and 30% CH_4 and calculated relative peak intensities of WC_{1-x} and W_2C phases.

patterns of the sample ***b*** are in good agreement with the calculated theoretical relative intensities and indicate that the tungsten carbide crystallites in the thin layer are randomly oriented.

A progressive amorphization occurs for films ***c***, ***d***, and ***e*** with a carbon concentration ranging between 62 and 77%; these films seem thus to be constituted by nanocrystalline WC_{1-x} grains in an amorphous carbon (a-C) matrix. Indeed, an increase in carbon concentration (i.e. an increase in the a-C matrix proportion) leads to a decrease of the number and size of the WC_{1-x} nanograins associated with the increase of the FWHM and the decrease of the peak intensities. No diffraction peaks were detected in the XRD patterns of W–C films deposited at CH_4 content higher than 5%.

GIXRD diagrams (figure 3) also exhibit large and asymmetric peaks. Three additional peaks in the 60° to 80° 2θ domain are observed, and they can be identified as the (220), (311) and (222) reflection peaks of the WC_{1-x} phase. With all GIXRD patterns having been recorded using the same parameters (such as slit size and x-ray beam intensity), and the samples having the same thickness, the diffracting volumes do not change and thus the intensities of the various diagrams are comparable.

First, the integrated peak intensities of sample ***b*** are higher than those of the other samples. Moreover, the relative intensities of the peaks are close to the calculated values (see table 2). These results confirm those obtained by XRD, i.e. this sample is constituted of WC_{1-x} nanograins randomly oriented.

The rather low intensity of the diffraction peaks in samples ***a***, ***c***, ***d***, ***e*** and ***f*** can be related to different origins. For sample ***a***, the XRD patterns show that the population of the (200) oriented nanograins is the most important. Due to the incident angle used in GIXRD incidence, the sole population of crystallites that could be in Bragg's position is the randomly oriented one. In sample ***a*** the population of these disoriented crystallites is lower than that of the sample ***b***, and thus the peak intensities are globally lower than the ones observed for sample ***b***. However, the intensities of (200), (220) and (311) peaks are higher than the theoretical ones reported

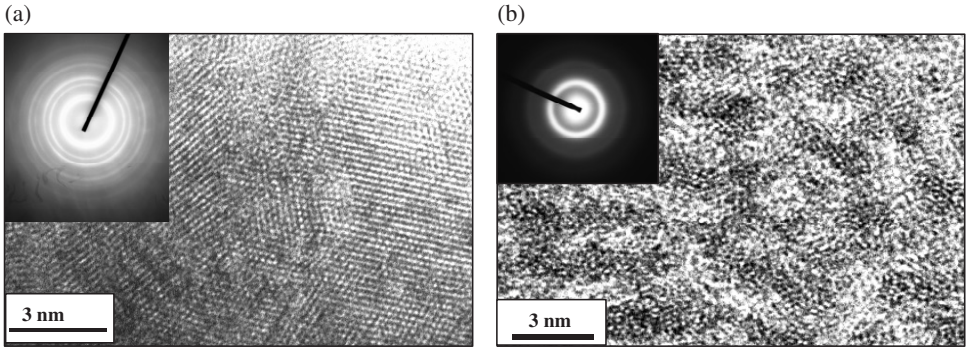

Figure 4. HRTEM images and electron patterns of coatings (a) b' and (b) e'.

in table 2. As a matter of fact, the (200) peak is around two times more intense than the (111) peak while it should be two times less intense. In addition, the (220) and (311) peak intensities are comparable to the (111) peak one, while it should be three times lower following our calculations. In GIXRD such modifications of the peak intensities can only be explained by a mixture of distinct phases. According to the composition of the film ($WC_{0.75}$), the W_2C phase could be present in this range of composition. The theoretical position of the W_2C phase peaks are thus reported in figures 2 and 3, and the position of the most intense (101) peak appears to be close to the (200) WC_{1-x} one, and this can explain the increase of the intensity in this part of the diagram. Similar explanations can be proposed for the (220) and (311) peaks of the WC_{1-x} phase which could overlap the (110) and (112) peaks of the W_2C phases. Then it seems reasonable to conclude that the sample $\boldsymbol{a}$ is constituted of a mixture of two phases: the WC_{1-x} phase with two populations of grains, one primarily (200) oriented and the other randomly oriented; and the W_2C phase randomly oriented.

For samples $\boldsymbol{c}$, $\boldsymbol{d}$, $\boldsymbol{e}$, and $\boldsymbol{f}$ the general tendency to amorphization decreases the amount and the size of the crystallized grains and leads then to the broad diffraction patterns which are observed. This effect increases with the amorphous carbon phase proportion, i.e. with the methane pressure during sputtering.

To complete this structural analysis, transmission electron microscopy analyses were carried out and they confirmed the main conclusions of the XRD experiments. Indeed the electron diffraction pattern of sample $\boldsymbol{b}'$ shows the diffraction planes corresponding to the WC_{1-x} phase and the HRTEM image exhibits WC_{1-x} nanocrystals with an average size close to 7 nm (figure 4(a)). These nanograins are close compact and no amorphous phase is visible at the grain boundaries. The HRTEM image obtained from sample $\boldsymbol{e}'$ shows a distribution of WC_{1-x} nanocrystallites (<3 nm) in an amorphous carbon matrix (figure 4(b)).

The nature of the chemical bonds in the films was studied by XPS, and figure 5 displays the C 1s XPS spectra recorded for $\boldsymbol{a}$, $\boldsymbol{b}$, $\boldsymbol{c}$, $\boldsymbol{d}$, $\boldsymbol{e}$, and $\boldsymbol{f}$. For the layers $\boldsymbol{a}$ and $\boldsymbol{b}$ formed at low methane pressures, the peaks of the C 1s core level show a single well defined component located at a binding energy BE = 283.6 eV. This value corresponds to those generally reported for the non-stoichiometric cubic WC_{1-x} phase [8, 15].

For the sample $\boldsymbol{f}$ obtained at the highest methane pressure in this work, the C 1s core level also has one component but it is located at 284.2 eV, a value corresponding to graphitic and amorphous hydrogenated carbon [27, 30]. For samples $\boldsymbol{c}$, $\boldsymbol{d}$ and $\boldsymbol{e}$, a progressive broadening of the C 1s core level can be observed. The deconvolution of these spectra shows two components: the first at 283.6 eV as observed for the samples $\boldsymbol{a}$ and $\boldsymbol{b}$, and the second located at 284.2 eV,

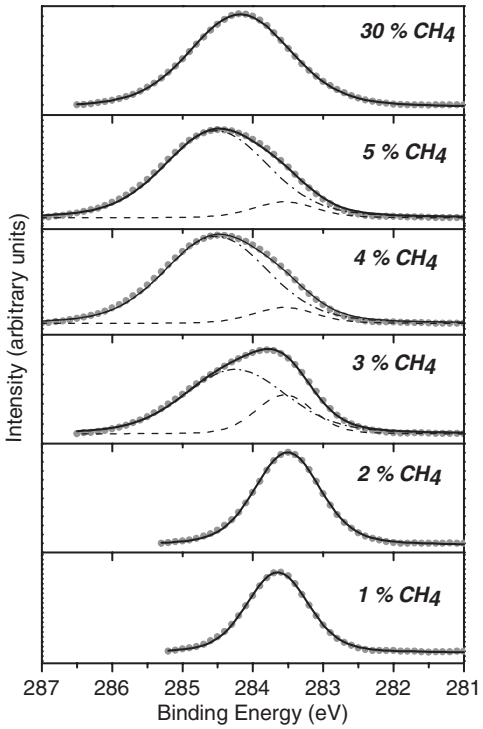

Figure 5. Superposition of the C 1s XPS spectra and their deconvolutions for films ***a***, ***b***, ***c***, ***d***, ***e***, and ***f***.

corresponding to graphitic carbon (C–C bonds) as observed for sample ***f***. The parameters of the deconvolution used (binding energy, FWHM, Gaussian/Lorentzian ratio) were imposed by the peaks obtained from the compounds being supposed pure (C 1s levels of samples ***b*** and ***f***).

Therefore, with increasing carbon content (from sample ***a*** to ***f***), the films transform from a WC_{1-x} composition to a WC_{1-x}/a-C phase mixture, and as a result the peak related to a-C increases whereas the peak (283.6 eV) due to the carbide phase gradually decreases.

Figure 6 shows the W 4f core levels for the various samples. A slight shift between the various spectra is observed (<0.2 eV). Since the shift is observed over the entire spectrum, it can be allotted to a slight change of the work function of the sample between the various samples. It thus seems that only one chemical form of W is observed. Based on the literature [24], a deconvolution procedure of the W 4f core levels was carried out (figure 7(a)), leading to two symmetrical components which could be attributed to a W–C bond and tungsten bonded to the residual oxygen (WO_2). However, the proportion of oxygen, after sputtering of the surface oxide layer, is negligible, as indicated by the decrease in the O 1s peak intensity. In addition, the W 4f line shape remains identical for the analysed samples, which means that the proportion of the oxide contribution would be constant for all the samples. This assumption remains not very probable because the intensity of the residual oxygen varies from one sample to another. Consequently an asymmetrical peak was selected to recompose the W 4f core levels.

The parameters of asymmetry used in the software ADVANTAGE are fixed at: tail mix = 30%, tail height = 0.01%, tail exponent = 0.12%. An example of recombining (sample ***b***) is given in figure 7(b).

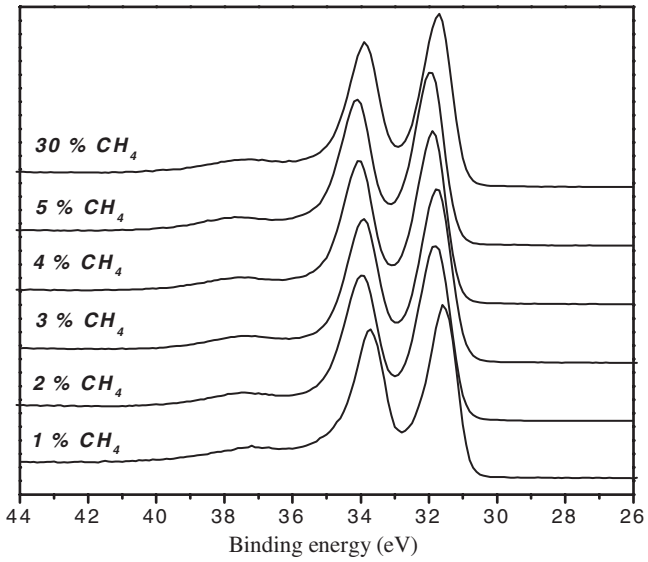

Figure 6. Superposition of the W 4f XPS spectra for films ***a***, ***b***, ***c***, ***d***, ***e***, and ***f***.

Table 3. Proportions of phases present in the W–C films ***a***, ***b***, ***c***, ***d***, ***e*** and ***f*** respectively deposited under 1, 2, 3, 4, 5 and 30% CH_4.

Sample	Phases present and their proportion	W_2C (%)	$WC_{0.88}$ (%)	a-C or a-C:H (%)
a	0.17 W_2C + 0.66 $WC_{0.88}$	21	79	0
b	1 $WC_{0.88}$ + 0 a-C + 0 W_2C	0	100	0
c	1 $WC_{0.88}$ + 0.77 a-C	0	56	44
d	1 $WC_{0.88}$ + 2.7 a-C	0	27	73
e	1 $WC_{0.88}$ + 4 a-C	0	20	80
f	1 a-C:H + trace of tungsten	0	0	100

The use of the asymmetrical peaks allows a valid deconvolution of all the samples. The intensity ratios of the W $4f_{7/2}$ and W $4f_{5/2}$ peaks is respected. This asymmetry is not yet explained. Nevertheless one can think that the metallic conduction with remaining intensity at the Fermi level observed for this material may lead to asymmetric peaks as is observed for pure metallic films.

From the RBS, XRD, GIXRD, TEM and XPS analyses, we can conclude that sample ***b*** is constituted of pure WC_{1-x} phase with a $WC_{0.88}$ composition. This composition has been further used to calculate the proportions of the different phases present in the films. It is worth noticing that since we have no reference sample constituted of the pure W_2C phase, we had to make the assumption that the W_2C phase composition is the one reported in the phase diagram (i.e. $WC_{0.5}$). The results are reported in table 3.

Thus the percentage of the phases has been calculated using the compositions, i.e., the WC_{1-x} phase having a composition of $WC_{0.88}$ and W_2C a composition of $WC_{0.5}$.

For example, the sample ***a*** with a composition of $W_1C_{0.75}$ is a mixture of both phases WC_{1-x} and W_2C; the percentage of phases is calculated as follows: $W_1C_{0.75} = xWC_{0.88} + yWC_{0.5} + z\text{a-}C$ (here $z = 0$).

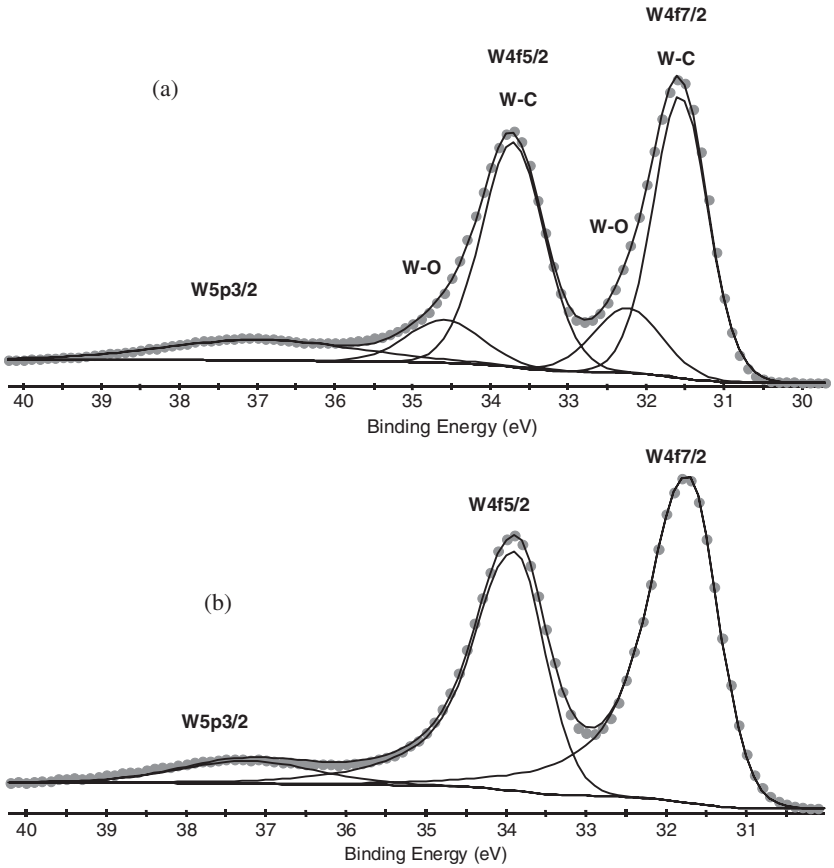

Figure 7. Deconvolution of the W 4f levels of the thin layer ***b***. (a) Deconvolution using two symmetrical components (according to the literature) and (b) deconvolution using an asymmetrical component.

3.2. Mechanical properties

The film ***b*** exhibits the maximum hardness (about 22 GPa). This value is close to the hardness of a WC bulk reference sample. Film ***a*** shows a slight lower hardness value of 19.5 GPa. As the carbon content increases (C/W $\gg$ 1) from 47 to 82%, the hardness of the W–C films decreases to 13 GPa. A lower hardness is observed for film ***f*** (5.51 GPa).

In our case, it appears that the most important factor that influences the coating's hardness is the phase composition. Figure 8 shows the variation of the hardness as a function of WC_{1-x} phase proportion in the thin films. Sample ***b*** is constituted by a single phase, i.e. WC_{1-x} with nanograins randomly oriented. Its hardness is the highest, while the other films, being constituted of a mixture of two phases, exhibit lower hardness.

Films ***c***, ***d***, and ***e*** contain a large concentration of carbon, with a grain size reduction, and thereafter, their hardness decreases rapidly with the amount of a-C phase. The hardness evolution in the region of WC_{1-x} + a-C mixture observed for these three samples is linear and suggests a mixture rule. Film ***f***, exhibiting an amorphous hydrogenated a-C phase, has the lowest hardness.

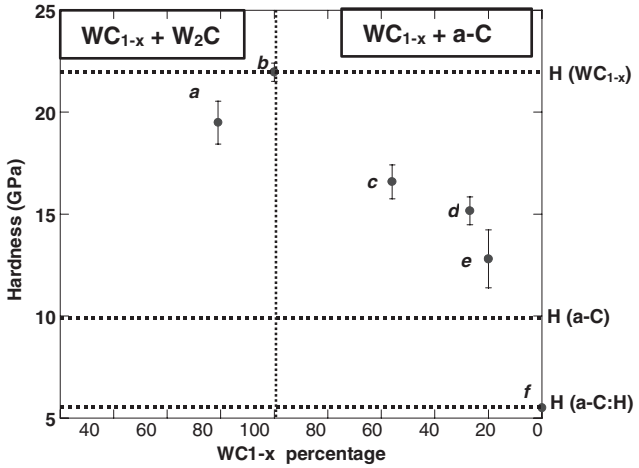

Figure 8. Variation of the hardness with phase proportion of coatings ***a***, ***b***, ***c***, ***d***, ***e***, and ***f***, respectively, deposited under 1, 2, 3, 4, 5 and 30% CH_4.

Film ***a*** contains the lowest percentage of carbon, but its hardness remains lower than the film ***b*** one; this difference may be due to the presence of a mixture of two phases: WC_{1-x} and W_2C.

The hardness of films is just one of the various parameters which play a crucial role in wear resistance. Protective films must also be highly resistant to plastic deformation during contact events. This requires a low Young's modulus E_r and high hardness since, according to Johnson's analysis, the load, P_y, needed to initiate plastic deformation when a rigid sphere of radius, r, is pressed into the coating is proportional to (H^3/E_r^2) [28, 29]. The ratio H^3/E_r^2 is a parameter which controls the resistance of materials to plastic deformation. This parameter was investigated as a function of the WC_{1-x} percentage (figure 9). Film ***b*** exhibits the higher resistance to plastic deformation (0.074); this is due to the fact that this film exhibits the higher hardness (22 GPa) and low Young's modulus ($E_r = 377$ GPa) compared to film ***a*** ($H = 19.5$ GPa; $E_r = 385$ GPa).

Films ***c***, ***d***, ***e***, have approximately the same resistance to plastic deformation (0.045) in spite of the difference in their hardness. Film ***f*** exhibits the lower plastic resistance parameter.

The friction coefficient increases slightly from 0.1 to 0.2 when the carbon content in the films increases. This slight increase in the friction coefficient of our films can be related to the difference of hardness diminishing the real contact area and reduced roughness of the surface. Indeed the very carbonaceous films are less hard; therefore, for the same normal force, the penetration depth is higher than in the case of hard films, which results to an increase of the resistance to the tip displacement during the scratch and leads to a higher coefficient of friction.

4. Conclusion

Nanocrystallized W–C films have been produced by reactive rf sputtering, using a tungsten target and methane gas. According to the carbon content, different phases have been observed.

- The sample formed at $P_{CH_4} = 1\%$ is constituted of a mixture of WC_{1-x} and W_2C phases.
- For $P_{CH_4} = 2\%$, the sample exhibits a pure WC_{1-x} phase.
- For $3\% \leqslant P_{CH_4} \leqslant 5\%$, nanocomposite WC_{1-x}/a-C has been observed.

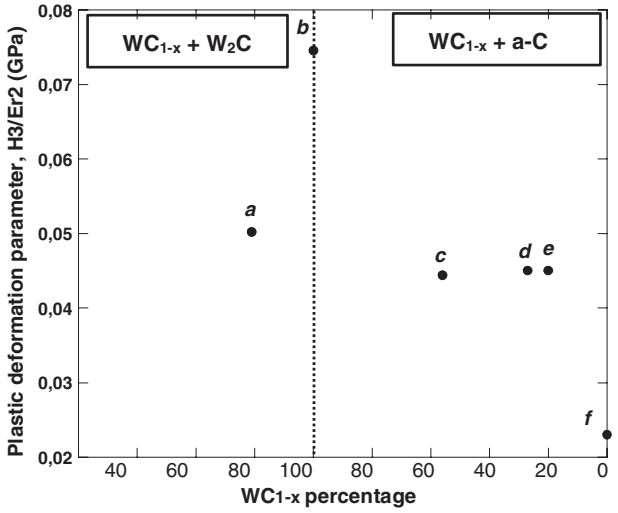

Figure 9. Plastic deformation parameter versus WC_{1-x} percentage in films $\boldsymbol{a}$, $\boldsymbol{b}$, $\boldsymbol{c}$, $\boldsymbol{d}$, $\boldsymbol{e}$, and $\boldsymbol{f}$.

- At $P_{CH_4} = 30\%$, the films are constituted by an amorphous hydrogenated carbon a-C:H phase.

The film exhibiting a pure WC_{1-x} phase with a composition close to $W_1C_{0.9}$ has the maximum hardness (22 GPa); this film also exhibits higher resistance to plastic deformation ($H^3/E_r^2 = 0.074$) and a lower friction coefficient (0.1). These properties are suitable for tribological applications.

Nanohardness measurements on the composite films ($\boldsymbol{c}$, $\boldsymbol{d}$ and $\boldsymbol{e}$) show a pronounced dependence on WC_{1-x} crystallite size and phase composition, both being a function of carbon content.

The observed mechanical behaviour seems to follow the simple rule of mixtures of hard and soft phases. At lower carbon concentration, the role of the soft phase is played by W_2C, whereas amorphous hydrogenated carbon phase contributes to composite softening at higher carbon content. Generally, the coatings exhibit a low friction coefficient (between 0.1 and 0.2).

The above conclusion can be summarized into one main conclusion, namely that the overall best mechanical and tribological properties are obtained for the film exhibiting a pure WC_{1-x} phase with a composition close to stoichiometry. Thus for the WC system a very precise control of the composition (i.e. of the deposition parameters) is necessary to obtain hard coatings.

Acknowledgments

The authors would like to thank G Renou and O Maciejak from Evry University for providing help during film deposition and nanohardness measurements, respectively.

References

[1] Toth L E 1971 *Transition Metal Carbides and Nitrides* (New York: Academic)
[2] Rudy E 1967 *J. Am. Ceram. Soc.* **50** 272
[3] Uhrenius B 1984 Calculation of the Ti–C, W–C, and Ti–W–C phase diagrams *CALPHAD* **8** 101–19
[4] Gustafson P 1986 Thermodynamic properties of the Co–W–C system *Mater. Sci. Technol.* **2** 653–8

[5] Toth L E 1971 *Transition Metal Carbides and Nitrides* (New York: Academic) p 85
[6] Demetriou Marios D, Ghoniem Nasr M and Lavine A S 2002 *J. Phase Equilib.* **23** 305–9
[7] Palmquist J P, Czigany Zs, Odén M, Neidhart J, Hultman L and Jansson U 2003 *Thin Solid Films* **444** 29–37
[8] Voevodin A A, O'Neil J P, Prasad S V and Zabinski J S 1999 *J. Vac. Sci. Technol.* **17** 986
[9] Srivastava P K, Vankar V D and Chopra K L 1985 *J. Vac. Sci. Technol.* A **3** 2129
[10] Srivastava P K, Vankar V D and Chopra K L 1986 *J. Vac. Sci. Technol.* A **4** 2819
[11] Gouy-Pailler Ph and Pauleau Y 1993 *J. Vac. Sci. Technol.* A **11** 96–102
[12] Cavaleiro A, Vieira M T and Lempériere G 1990 *Thin Solid Films* **185** 199–217
[13] Keller G, Barzen I, Dotter W, Erz R, Ulrich S, Jung K and Ehrhardt H 1991 *Mater. Sci. Eng.* A **139** 137–43
[14] Machida K, Enyo M and Toyoshima I 1988 *Thin Solid Films* **161** L91–5
[15] Rinçon C, Zambrano G, Carvajal A, Prieto P, Galindo H, Matinez E, Lousa A and Esteve J 2001 *Surf. Coat. Technol.* **148** 277–83
[16] Radic N, Pivac B, Meinardi F and Koch Th 2005 *Mater. Sci. Eng.* A **396** 290–5
[17] Zambrano G, Riascos H, Prieto P, Restrepo E, Devia A and Rinçon C 2003 *Surf. Coat. Technol.* **172** 144–9
[18] Bewilogua K and Dimigen H 1993 *Surf. Coat. Technol.* **61** 144–50
[19] Esteve J, Zambrano G, Rinçon C, Martinez E, Galindo H and Prieto P 2000 *Thin Solid Films* **373** 282–6
[20] Pauleau Y and Gouy-Pailler Ph 1992 *J. Mater. Res.* **7** 2070–9
[21] Van Dyun W and Van LchemàLochem B 1989 *Thin Solid Films* **181** 497–503
[22] Srivastava P K, Vankar V D and Chopra K L 1988 *Thin Solid Films* **161** 107–16
[23] Rinçon C, Romeo J, Esteve J, Martinez E and Lousa A 2003 *Surf. Coat. Technol.* **163/164** 386–91
[24] Monteiro O R, Deplancke-Ogletree M P D, Yu Lo R, Winand R and Brown I 1997 *Surf. Coat. Technol.* **94/95** 220–5
[25] Wang D Z, Chen J X, Zhang H L and Huang N K 2000 *Nucl. Instrum. Methods Phys. Res.* B **171** 465–9
[26] Oliver W C and Pharr G M 1992 *J. Mater. Res.* **7** 1564
[27] Luthin J and Linsmeier Ch 2000 *Surf. Sci.* **454–456** 78–82
[28] Musil J, Kunc F, Zeman H and Polakova H 2002 *Sur. Coat. Technol.* **154** 304–13
[29] Tsui T Y, Pharr G M, Oliver W C, Bhatia C S, White R L, Anders S, Anders A and Brown I G 1995 Mechanical behavior of diamond and other forms of carbon *Mater. Res. Soc. Symp. Proc.* **383** 447
[30] Li G and Xia L F 2001 *Thin Solid Films* **396** 16–22